Upslope Internal-Wave Stokes Drift, and Compensating Downslope Eulerian Mean Currents, Observed above a Lakebed

STEPHEN M. HENDERSON

School of the Environment, Washington State University, Vancouver, Washington

(Manuscript received 26 June 2015, in final form 14 January 2016)

ABSTRACT

In a small lake, where flows were dominated by internal waves with 10–32-h period, slow but persistent mean transport of water over many wave periods was examined. Acoustic Doppler profilers (ADPs) and a vertical string of temperature loggers were deployed where the lower thermocline intersected the sloping lakebed. Near (<1 m above) the bed, internal waves, coherent with a lakewide seiche, propagated upslope at ~0.023 m s^{-1}. Near-bed wave-induced water velocity fluctuations had a standard deviation of <0.02 m s^{-1}. Near the surface, velocity fluctuations had similar magnitude, but lateral wave propagation was unclear. Averaged over many wave periods, the near-bed Eulerian velocity flowed downslope at ~0.01 m s^{-1}, and was roughly cancelled by an upslope internal-wave Stokes drift (estimated by assuming that weakly nonlinear waves propagated without change of form). To examine net transport, while relaxing approximations used to estimate the Stokes drift, the observed temperature range (9°–25°C) was divided into 0.5°C increments, and the depth-integrated, wave-averaged flux of water in each temperature class was calculated. The coldest (near-bed) water was slowly transported onshore, opposite the Eulerian mean velocity. Onshore flux of warm near-surface water was comparable to an Eulerian-mean flux, indicating minimal near-surface Stokes drift. Intermediate water, from the middle of the water column and the outer boundary layer, was transported offshore by an offshore Stokes drift. The downslope near-bed Eulerian mean velocity, together with intensification of mean stratification within 0.4 m of the bed, may enhance boundary layer mixing.

1. Introduction

Ecosystems in lakes, estuaries, and oceans are shaped by water flows that advect heat, salinity, sediments, nutrients, pollutants, and organisms. Advection is sometimes complicated by flow reversals associated with internal waves. This paper is devoted to analysis of mean advection in the presence of internal waves.

Advection has been quantified by tracing the movement of plankton, drifters, dye, or other chemicals. Such tracer observations have yielded valuable insights, such as quantifying mixing rates in lakes, estuaries, and oceans (Ledwell et al. 1993; Goudsmit et al. 1997; Inall 2009; Wain and Rehmann 2010) and showing that internal waves sometimes advect plankton considerable distances in the coastal ocean (Pineda 1999). However, in shallow environments, individual tracer patches are often followed for only a limited period, making quantification of long-term mean advection difficult. This paper presents observations collected continuously over two months, to identify persistent advection in a stratified lake over many internal wave periods.

Observations were collected using stationary instruments, which are convenient for prolonged deployments. Unfortunately, when averaged over internal wave periods, the Eulerian velocity at a fixed point, which is easily calculated from such observations, differs from the Lagrangian velocity experienced by moving water particles. The difference between wave-averaged Eulerian and Lagrangian velocities is called the Stokes drift (Phillips 1977, his section 3.3). Theoretical expressions for the Stokes drift have been derived for a variety of nondissipative internal waves, including gravity wave modes propagating normal to a sloping bed (Wunsch 1971), oblique planar inertio-gravity waves reflecting from a sloping bed (Thorpe 1997), wave beams reflecting from the ocean

Denotes Open Access content.

Corresponding author address: Stephen M. Henderson, School of the Environment, Washington State University, 14204 NE Salmon Creek Ave., Vancouver, WA 98686.
E-mail: steve_henderson@wsu.edu

DOI: 10.1175/JPO-D-15-0114.1

surface (Tabaei et al. 2005; Zhou and Diamessis 2015), and equatorial Kelvin waves (Weber et al. 2014). Here, two different techniques are used to quantify transport in the presence of substantial internal-wave Stokes drift. The field site and instrumentation are described in section 2, and the methods used to examine persistent transport are explained in sections 3 and 4. Significant internal wave Stokes drift has previously been measured over the continental shelf (Huthnance 1995; Inall et al. 2001; Zhang et al. 2015). However, results presented here are novel in resolving Stokes drift through the internal wave bottom boundary layer (BBL), and in extending Stokes drift measurement to lake environments. Additionally, these measurements highlight an interaction between the Stokes drift and the Eulerian mean flow near the sloping bed, discussed below.

The waves considered here were coherent with a lakewide internal seiche. Near the sloping lakebed, the waves propagated upslope as pitched-forward internal bores (section 5a). Farther above the lakebed, waves were less borelike, and lateral propagation was unclear. The Stokes drift was estimated throughout the BBL, under assumptions of weak nonlinearity and steady upslope wave propagation, from vertical profiles of velocity measured using fixed acoustic Doppler profilers (ADPs). BBL Stokes drift was directed upslope and was partially canceled by a downslope Eulerian mean flow (section 5b). Models that neglect mixing provide a simple explanation for this observation: since persistent upslope (downslope) particle motion would advect steadily cooler (warmer) water past a fixed location, Eulerian and Stokes transports must cancel in the steady state (Wunsch 1971; Ou and Maas 1986; Thorpe 1997). Upslope wave propagation is common in lakes (Imberger 1998) and oceans (Klymak and Moum 2003; Hosegood and van Haren 2004; Bluteau et al. 2011; Walter et al. 2014), and upslope near-bed Stokes drift is a general property of upslope propagation (section 3), so the behavior measured here might occur in other environments. Direct field measurement of the partial cancelation of Eulerian and Stokes transports is novel, although observations of internal tidal rectification over continental slopes have yielded potentially analogous results. Specifically, some near-bed observations (Butman 1988; Pingree and Le Cann 1989) have revealed downslope Eulerian-mean velocities and upslope Eulerian-mean wave-generated density fluxes (such fluxes, equal to the covariance between tidal-frequency fluctuations in density and upslope velocity, may be associated with the Stokes drift; Middleton and Loder 1989).

The approximate cancellation between estimated Stokes and Eulerian transports presented here provides a simple explanation of leading-order mean velocities in the BBL. However, it is departures from perfect cancellation that represent persistent advection. If net advection were calculated as a small difference between large Eulerian and Stokes transports then severe errors could result, particularly given the small-amplitude approximation used to estimate the Stokes drift. Furthermore, the calculation of the Stokes drift discussed above required an assumption of steady (upslope) wave propagation, but clear wave propagation was observed only near the bed. Therefore, net transport was estimated using a second, alternative, approach resembling analysis previously used to identify eddy-averaged transport in isopycnal-coordinate ocean models (McDougall and McIntosh 2001) and tidally averaged transport in field observations [e.g., MacDonald 2006; MacCready (2011) calculated transport in estuaries, and Bryden et al. (1994) estimated transport through the Strait of Gibraltar]. Persistent advection was separated from wave-induced fluctuations by partitioning water into temperature classes and calculating the depth-integrated transport of water for each class, averaged over several wave periods. Under certain approximations, the resulting ''isothermal mean'' transport is proportional to the mean particle velocity (section 4). As expected given near-cancellation of Eulerian and Stokes transports, mean transport of the coolest (near bed) temperature classes was smaller than would occur if particles simply moved with the Eulerian-mean velocity (section 5c).

Mean advection was evaluated throughout the water column. The discussion (section 6) focuses on near-bed advection, because models suggest that such advection might influence the effectiveness of BBL mixing. In the absence of waves, steady-state models that account for BBL mixing predict upslope transport of the densest water in the inner boundary layer and downslope transport of lighter water in the outer boundary layer (Phillips et al. 1986; Garrett et al. 1993). BBL models that simulate wave-induced velocity fluctuations, but neglect the Stokes drift, yield similar predictions for the mean velocity profile (Umlauf and Burchard 2011). Simulated advection is vital to continued mixing: sheared BBL currents tilt isotherms to maintain stratification, and therefore turbulent buoyancy fluxes, in the presence of ongoing mixing. However, given a mixing-induced reduction of inner-BBL stratification, simulated flows also advect buoyancy countergradient (when integrated across a horizontal plane enclosing the BBL), partially canceling turbulent mixing (Garrett et al. 1993). These predictions, obtained using models that neglect wave-induced fluxes, are compared with BBL advection and stratification observed here in the presence of wave-induced fluxes. Potential implications for BBL mixing and sediment transport are noted.

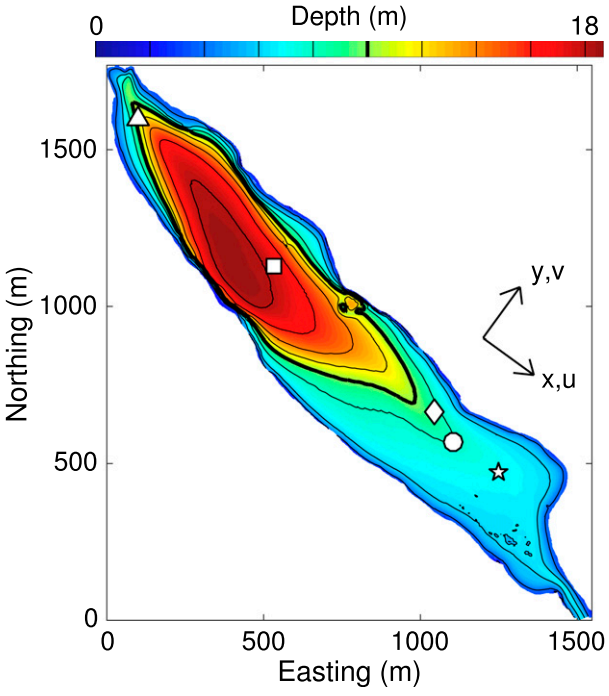

FIG. 1. Lacamas Lake bathymetry and locations of tripod (circle), deep water temperature profile (square), and additional Hobo temperature loggers (triangle, diamond, and star). Arrows show directions of along-lake coordinate x and velocity u, together with across-lake coordinate y and velocity v. Northing and easting measured from 45.60977°N, 122.43667°W.

2. Field site and instrumentation

Measurements were collected using fixed instruments deployed in Lacamas Lake, Washington (Fig. 1), from 18 May to 18 July 2012 (Deemer et al. 2015). Quality control led to elimination of some velocity data from early and late in the deployment, so velocities from 24 May to 11 July were selected for presentation here. Velocities in this lake are dominated by fluctuations of a few centimeters per second, with periods on the order of 1 day. These velocity fluctuations result from internal waves resembling high-vertical-mode internal seiches; horizontal wavelengths are about twice the lake length, and vertical wavelengths are less than the water depth (Henderson and Deemer 2012). Wave phases propagate upward and energy propagates downward, owing to wave dissipation in the BBL (Henderson and Deemer 2012; Henderson 2016). This vertical seiche propagation contrasts with the vertically standing modes that result when energy is strongly reflected from the surface and the lakebed [for a review of internal waves in lakes, including nondissipative seiches, see Boegman (2009)]. Near the thermocline, the wave's vertical phase speed c_z fits the linear theory prediction

$$c_z = 2\pi\sigma^2\lambda_x/\langle N\rangle, \quad (1)$$

where σ is the wave frequency, $\lambda_x = 3000$ m is the horizontal wavelength at the depth of the thermocline, the buoyancy frequency $\langle N\rangle = [-(g/\langle\rho\rangle)\partial\langle\rho\rangle/\partial z]^{1/2}$, the water density ρ is calculated from water temperature, and angle brackets $\langle\cdot\rangle$ denote an average over sufficient time to remove wave fluctuations (taken above as the entire deployment duration, and taken in formulas introduced below as either two days or the entire deployment duration). The Coriolis force is absent from (1) because the narrowness of Lacamas Lake ensures dominance of along-lake velocities. The force required to prevent Coriolis from deflecting flow away from the along-lake axis is provided by across-lake baroclinic pressure gradients (i.e., an approximate across-lake thermal wind balance is observed; Henderson and Deemer 2012).

Within about 1 m of the sloping bed of Lacamas Lake, 1°–3°C seiche-induced temperature fluctuations are characterized by long intervals of slow warming, punctuated by short intervals of rapid cooling. The sudden cooling events mark arrival of the pitched-forward front faces of near-bed internal bores (Deemer et al. 2015). Farther above the bed, waves are more sinusoidal (Henderson and Deemer 2012; see also section 5a herein). Since bores are confined to the near-bed region, they likely result from internal wave shoaling and boundary layer processes (Thorpe 1992, 1999; Hosegood and van Haren 2004; Boegman et al. 2005a) rather than from the midbasin nonlinear steepening (Thorpe 1971, 1974; Boegman et al. 2005b) that is often important for larger-amplitude seiches (Horn et al. 2001). Since bore thickness is comparable to BBL thickness, turbulent mixing and dissipation may influence bore dynamics. Bores are often observed near sloping beds of lakes (Imberger 1998; Thorpe and Lemmin 1999; Cossu and Wells 2013) and oceans (Bluteau et al. 2011; Walter et al. 2014).

Above the turbulent BBL, which extends about 0.4–1 m above the bed of Lacamas Lake (Deemer et al. 2015; Henderson 2016), stratification strongly inhibits mixing (gradient Richardson numbers are consistently above 1; see section 5a). Within the BBL, sheared upslope and downslope flows induce periodic fluctuations in stratification by tilting isotherms. This "shear-induced periodic stratification" (Lorke et al. 2005) elevates vertical gradients in temperature (and in concentrations of ecologically important chemicals such as NO_3^- and N_2O) during downslope flow, and reduces gradients during upslope flow (Deemer et al. 2015).

Velocity was measured by three 2-MHz Nortek Aquadopp ADPs mounted on an aluminum tripod

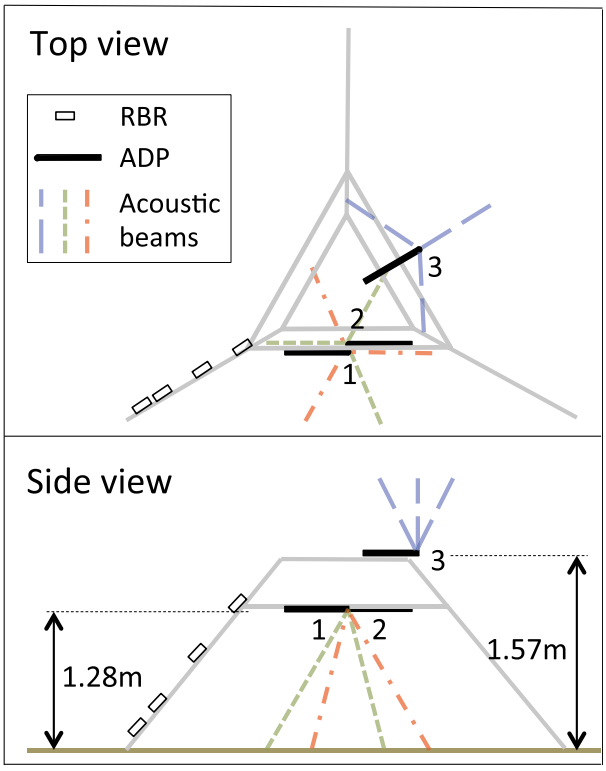

FIG. 2. Instrument configuration on tripod. Gray lines indicate aluminum tripod, unfilled squares indicate RBR temperature loggers, and black bars labeled 1–3 respectively indicate downward ADPs 1–2 and upward ADP 3. Red dotted-dashed, green short-dashed, and blue long-dashed lines respectively indicate the acoustic beams of these three ADPs.

(Fig. 2). The tripod was deployed in about 8-m depth on the sloping lakebed (~0.86° slope, up toward southeast) at 45.61515°N, 122.42268°W (circle, Fig. 1). Two ADPs were mounted at elevation $z \approx 1.3$ m above the bed, pointed downward to measure velocity every 0.015 m from $z = 0.135$ m to $z = 1.14$ m (Fig. 2). At $z < 0.135$ m, velocity measurements may have been contaminated by acoustic sidelobe reflections from the bed, and were neglected. The third ADP was deployed at $z \approx 1.6$ m, pointed upward to measure velocity every 0.33 m along a vertical profile extending from $z \approx 2.23$ m to the water surface. Velocities measured within 0.33 m of the surface were neglected.

The two downward-looking ADPs operated in pulse-coherent mode (Lohrmann et al. 1990), with a long (6.8 m) pulse-to-pulse distance yielding high-resolution, low-noise measurements. One ADP, used for all results presented in section 5, recorded one 1-s burst of two 0.5-s-averaged measurements every 12 s. The second downward-looking ADP, used here only to assess measurement accuracy, sampled a single 0.5-s-averaged velocity every 30 s. Low (<75%) correlation data were removed, and remaining data were averaged to calculate hourly mean velocities at every elevation throughout the 48-day deployment. The two downward-looking ADPs were in excellent agreement. Let $[u_1(t), v_1(t)]$ and $[u_2(t), v_2(t)]$ be hourly mean velocity time series measured at the same elevation by the two ADPs. At every elevation between 0.135 and 0.8 m, linear regression yielded $u_1 + iv_1 = Ae^{i\psi_1}(u_2 + iv_2) + b$ with $0.997 < A < 1.012$, $1° < \psi_1 < 3°$, $|b| < 2.2 \times 10^{-4}$ m s^{-1}, and correlation coefficient $r^2 > 0.99$. Nearer the instruments, agreement degraded a few percent, perhaps owing to disturbance of flow by the instruments (A remained within 2% of 1, r^2 remained greater than 0.99, and $|b|$ remained $<3 \times 10^{-4}$ m s^{-1}). The third, upward looking, ADP recorded one-minute-averaged velocity every minute throughout the deployment, sampling in standard (not pulse-coherent) mode. From the high-frequency noise floor in velocity spectra, noise in minutely velocity for the upward ADP was estimated as 0.03 m s^{-1}, roughly consistent with manufacturer's estimates. Scatter in time-averaged ADP velocity errors scales with (averaging time)$^{-1/2}$, so random errors in the hourly, 48-hourly, and 48-day means considered below are respectively 4×10^{-3}, 6×10^{-4}, and 1×10^{-4} m s^{-1} for the upward ADP. These errors will prove insignificant compared with observed velocities. Owing to more accurate pulse-coherent sampling (Lohrmann et al. 1990), random errors for the downward ADP were smaller. Bias, as might for example result from misalignment of acoustic beams, was likely a more significant source of error but cannot be estimated from scatter in measurements from a single instrument. The regression noted above between redundant downward ADP measurements suggests that bias for these instruments was $<2.2 \times 10^{-4}$ m s^{-1}, which will prove small compared with observed velocities.

At the tripod deployment site, temperature was measured using Richard Brancker Research Ltd. (RBR) XR-1060 fast-response loggers at $z = 0.2$, 0.4 m (mounted on tripod leg, recording every 2 s, error < 0.01°C), RBR XR-420 CT loggers at $z = 0.9$, 1.3 m (mounted on tripod leg, recording every 10 s, error < 0.01°C), and Onset Hobo Pro V2 loggers at $z = 2.1$, 4.3, 5.8, and 7.3 m (mounted on cable extending up from tripod, recording every 4.25 min, error < 0.2°C).

Temperature was measured at four additional locations in the lake. One Hobo was deployed 16 June–18 July, about 3 m above the bed in about 10-m depth near the lake's northwest end (triangle, Fig. 1). Two near-bed Hobos ($z \approx 0.3$ m) were deployed 16 June–18 July, downslope (45.61600°N, 122.42350°W; diamond, Fig. 1) and upslope (45.61428°N, 122.42080°W; star, Fig. 1) of the tripod. About 100 m from the lake's deepest point (45.62003°N, 122.43023°W; square, Fig. 1),

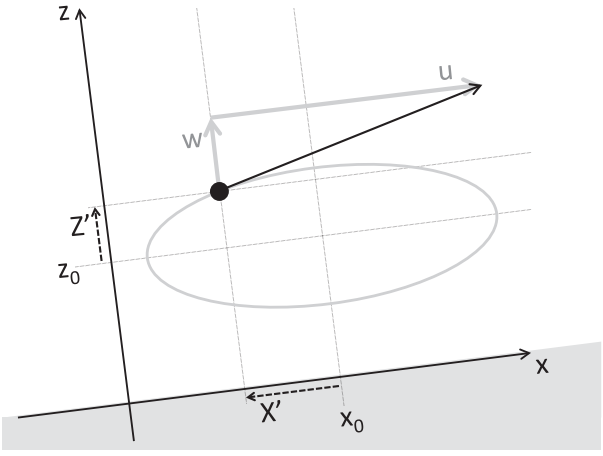

FIG. 3. Definition sketch showing coordinates (x, z) and path (gray ellipse) of a water particle oscillating about wave-averaged location (x_0, z_0). Black dot shows an example of instantaneous particle location, with associated velocity (u, w) and displacement (X', Z'). Closed particle orbit (ellipse) drawn for simplicity; actual particle motion may progress to right if Lagrangian-mean velocity $\langle u \rangle + u_{ST} > 0$, or left if $\langle u \rangle + u_{ST} < 0$.

in about 17-m depth, temperature profiles were measured on 18 May and 11 July by lowering a Hach DS5X Sonde (error < 0.15°C).

3. Stokes drift

Previous theoretical expressions for the Stokes drift for nondissipative internal waves (Wunsch 1971; Thorpe 1997; Tabaei et al. 2005; Weber et al. 2014) are not valid in the dissipative BBL. Next, expressions are presented for calculation of the BBL Stokes drift from observed velocity profiles (section 3a). The following is based on previous analysis of general (Middleton and Loder 1989) and surface-wave BBL (Longuet-Higgins 1953) cases, and also has similarities to Lamb (1997). Expressions are presented in a form that highlights simple qualitative properties of the internal wave Stokes drift (section 3b) while facilitating comparison with alternative isothermal-mean analysis (section 4).

a. Quantitative evaluation of the Stokes drift

Let (x, z) be upslope and bed-normal coordinates, with $z = 0$ at the bed (Fig. 3). Consider a water particle moving back and forth with each wave, with a wave-averaged location (x_0, z_0). Let (u, w) be (x, z) components of velocity. For simplicity, velocity perpendicular to (u, w) will be neglected in all wave-averaged transport calculations. This assumption is motivated by the dominance of along-lake velocities in Lacamas Lake, but may be a poor approximation in basins characterized by three-dimensional motions (e.g., Poincare modes). Let Δu be the difference between u for the moving particle and u at (x_0, z_0). Now Δu fluctuates through each wave cycle, but its persistent mean value $\langle \Delta u \rangle = u_{ST}$ is the Stokes drift. For weakly nonlinear, statistically steady waves, given mean velocity gradients not greatly exceeding gradients in wave-frequency velocity, it can be shown (see the appendix) that

$$u_{ST} \approx \frac{\partial \langle u' Z' \rangle}{\partial z}, \tag{2}$$

where Z' is the particle's boundary-normal displacement from z_0 (throughout, primes indicate departures from wave-averaged values). Interpretation of (2) is discussed in section 4b.

For field application of (2), profiles of u can be measured using ADPs. It remains to estimate Z'. In principle, leading-order Z' can be calculated by time-integrating ADP measurements of w', but w' may be unmeasurably small. An alternative approach, used here, is to assume that waves propagated upslope at phase speed c ($c < 0$ for downslope propagation) while changing their form only slowly, so u is locally a function of $x - ct$, leading to

$$Z'(z) \approx \frac{1}{c} \int_{\tilde{z}=0}^{z} u' \, d\tilde{z}, \tag{3}$$

which can be evaluated from ADP profiles. To derive (3), note that $\partial u/\partial x \approx -c^{-1} \partial u/\partial t$ for steadily propagating waves, so the mass conservation equation $\partial u'/\partial x + \partial w'/\partial z = 0$ becomes $\partial w/\partial z \approx c^{-1} \partial u/\partial t$. Integrating over time yields $\partial Z'/\partial z \approx u/c$ at leading order, and integrating vertically from the bed yields (3). For $z < 0.135$ m, where ADP measurements were unreliable, velocity was estimated by assuming a logarithmic profile, that is,

$$u(z) = u|_{z=0.135\,\mathrm{m}} \frac{\log(z/\hat{z})}{\log(0.135/\hat{z})}, \tag{4}$$

where $u|_{z=0.135\,\mathrm{m}}$ denotes u evaluated at $z = 0.135$ m, and the roughness length $\hat{z} = 10^{-3}$ m (results were insensitive to $\hat{z}$ between 10^{-5} and 10^{-1} m). Each hour, (3) was evaluated by analytic integration of (4) from $\hat{z}$ to 0.135 m, and trapezoidal integration of ADP profiles above 0.135 m.

b. Qualitative properties of the Stokes drift

Consider a rigid-lid internal wave propagating in constant depth h. Now the depth-integrated Stokes drift equals zero [because $Z' = 0$ at the surface and at the bed, and from (2), $\int_0^h u_{ST} \, dz = \langle uZ' \rangle|_{z=h} - \langle uZ' \rangle|_{z=0}$; see also Weber et al. (2014)]. Therefore, reversals in Stokes drift along vertical profiles, noted by many authors (Thorpe

1997; Weber et al. 2014), are expected. For the case of a nondissipative mode-1 internal wave propagating upslope, Stokes drift is directed toward shallow water near the bed and near the surface, with a reversal in the midwater column (Wunsch 1971; see also section 4b herein).

The near-bed Stokes drift transports water in the direction of wave propagation, as can be proved by substituting (3) into (2) to yield

$$u_{\mathrm{ST}} = \left\langle \frac{\partial u'}{\partial z}\left(\frac{1}{c}\int_{\tilde{z}=0}^{z} u'\,d\tilde{z}\right)\right\rangle + \frac{\langle u'^2\rangle}{c}. \tag{5}$$

The second term of (5) always contributes drift in the direction of wave propagation. Through much of the BBL, $|u|$ increases with z, and $\partial u/\partial z$ tends to have the same sign as $\int_{\tilde{z}=0}^{z} u\,d\tilde{z}$ (because boundary layer phase shifts are usually less than 90°), so the first term reinforces the second.

From the above discussion, the Stokes drift of propagating internal waves flows in the direction of wave propagation near the bed, with at least one reversal higher in the water column.

4. Estimation of transport in isothermal coordinates

In this section, an alternative isothermal-mean view of advection is outlined. Following MacDonald (2006), McDougall and McIntosh (2001), and many others, an isothermal-mean transport $q(T)$ is defined, representing the wave-averaged lateral flux of water with temperatures near T (section 4a). For cases of negligible mixing, (and under simplifying assumptions), proportionality between $q(T)$ and particle (Eulerian plus Stokes) velocity is noted (section 4b). As clarified in section 4b, this analysis uses temperature to trace vertical motion (cf. Pinkel et al. 2012), allowing relaxation of the assumptions (steady propagation and weak nonlinearity) that were required in section 3. Even in cases with rapid turbulent mixing, for which temperature is not a tracer of wave-induced motion, boundary layer–averaged Lagrangian-mean velocities can be recovered if mixing is confined to the BBL (section 4b).

Measured hourly mean velocities are expected to be predominantly bed-parallel near the bed, and surface-parallel near the water surface. For the analysis of near-bed flows in section 3, coordinates (x, z) were defined as bed-parallel and bed-normal. Given the small bed slope (0.86°), bed-parallel and bed-normal coordinates may be indistinguishable from horizontal and vertical coordinates when analyzing current meter data. The distinction between coordinates is neglected in the following analysis, which addresses only the dominant, lateral component of the flow.

a. Definition of isothermal-mean transport

Divide the range of measured temperatures into closely spaced increments centered on T_1, T_2, T_3, ... such that $T_{j+1} = T_j + \Delta T$. Let $\Delta q(T_j)$ be the depth-integrated, wave-averaged volume flux of all water with temperatures between $T_j - \Delta T/2$ and $T_j + \Delta T/2$. Since $\Delta q(T_j)$ is proportional to ΔT, it will be convenient to work with $q(T_j) = \Delta q(T_j)/\Delta T$ (with units $\mathrm{m^2\,s^{-1}\,°C^{-1}}$), which equals

$$q(T_j) = \int_{z=0}^{h} \mathscr{T}(T_j, z)\,dz, \tag{6}$$

where

$$\mathscr{T}(T_j, z) = \langle \delta[T(t,z) - T_j]u(t,z)\rangle, \tag{7}$$

and the time average in (7) is effectively limited to the jth temperature class by the delta function

$$\delta[T(t,z) - T_j] = \begin{cases} \Delta T^{-1} & |T(t,z) - T_j| < \Delta T/2 \\ 0 & \text{otherwise} \end{cases}. \tag{8}$$

The function $\mathscr{T}(T, z)$ partitions flux into temperature and elevation classes. Integrating $\mathscr{T}(T, z)$ over z gives depth-integrated transport in a temperature class [(6); it can also be shown that integrating $\mathscr{T}(T, z)$ over T gives the Eulerian mean velocity at fixed z]. For given T_j, the range of depths in which $\delta[T(t, z) - T_j]$ is nonzero moves up and down as isotherms are displaced by internal waves, but the horizontal location at which the integral (6) is evaluated is fixed, and does not move laterally with water particles.

Isothermal-mean fluxes were evaluated at the tripod location using ADPs and the vertical string of temperature gauges. At each temperature gauge elevation, $\delta[T(t, z) - T_j]$ was evaluated from hourly mean temperature and (8) with temperature resolution $\Delta T = 0.5$°C, and $u(z, t)$ was evaluated by linearly interpolating (in z) ADP hourly mean velocity profiles. $(T_j, 0)$ was set to zero, and (T_j, h) was set equal to the value estimated at the highest temperature gauge. Vertical trapezoidal integration of the $\mathscr{T}(T_j, z)$ values estimated at temperature logger locations was then used to evaluate (6).

b. Relation between isothermal-mean transport and particle velocity

Let $Z_T = \langle Z_T\rangle + Z'_T$ be the elevation of the temperature-T isotherm [following McDougall and McIntosh (2001), Z_T is set to 0 (or h) whenever T is colder (or warmer) than all temperatures observed in the water column]. A vertical profile of thickness-weighted isothermal-mean transport velocity u_T is defined such that the

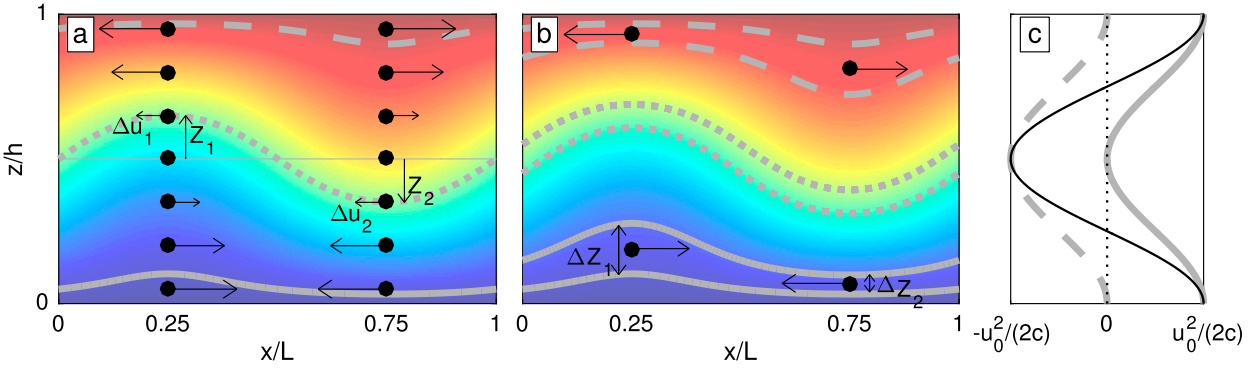

FIG. 4. Stokes drift for a nondissipative linear internal wave with zero Eulerian mean flow (amplitude exaggerated). (a) The nonbolus contribution to Stokes drift u_{nb}. Cross section shows a snapshot of temperature (color), isotherms (gray lines), and horizontal velocity (arrows) for a mode-1 wave of wavelength L propagating in direction $+x$ with phase speed c and maximum velocity amplitude u_0. At $x/L = 0.25$, shear is negative ($\partial u'/\partial z < 0$), so upward displacement ($Z_1 > 0$) carries intermediate-temperature water (dotted gray line) into a region of leftward flow ($\Delta u_1 < 0$). At $x/L = 0.75$, both shear and displacement reverse ($\partial u'/\partial z > 0, Z_2 < 0$), so intermediate-temperature water is again in a region of leftward flow ($\Delta u_2 < 0$). The velocity averaged along the moving isotherm is $\langle u\rangle + u_{nb}$, which equals u_{nb} in this case because the Eulerian-mean velocity $\langle u\rangle = 0$. Approximating velocity with a linear function of depth yields $u_{nb} = \langle(\partial u'/\partial z)Z_T'\rangle < 0$. For near-bed and near-surface waters (solid and dashed gray lines), u_{nb} is small, because Z_T' and $\partial u'/\partial z$ are small. (b) The bolus velocity u_b. A cold near-bed water layer, bounded by solid gray isotherms, is thicker at $x/L = 0.25$, where flow is to right, than at $x/L = 0.75$, where flow is to left (i.e., $\Delta Z_1 > \Delta Z_2$). A rightward "bolus flux" results. Letting $\overline{\Delta Z}$ = mean thickness, the instantaneous thickness is approximately $\overline{\Delta Z}(1 + \partial Z_T'/\partial z)$, the mean bolus flux is $\overline{\Delta Z}\langle u'\partial Z_T'/\partial z\rangle > 0$, and the mean bolus velocity is $u_b = \langle u'\partial Z_T'/\partial z\rangle > 0$ (the Eulerian flux $\overline{\Delta Z}\langle u\rangle = 0$ in this case). A warm near-surface layer (bounded by dashed lines) experiences a similar bolus velocity. An intermediate layer (bounded by dotted lines) has the same thickness at $x/L = 0.25$ as at $x/L = 0.75$, and experiences no bolus velocity. (c) Vertical profile u_{nb} (dashed gray), u_b (solid gray), and $u_{ST} = u_{nb} + u_b$ (black line).

flux $(\langle Z_{T+dT}\rangle - \langle Z_T\rangle)u_T$ attributed to elevations between $\langle Z_T\rangle$ and $\langle Z_{T+dT}\rangle$ equals the flux $q(T)dT$ of water with temperatures between T and $T + dT$, leading to

$$u_T = \frac{q(T)}{\partial\langle Z_T\rangle/\partial T}. \tag{9}$$

To separate wave-induced temperature fluctuations from seasonal warming, angle brackets here represent only short (2 day) averages, rather than averages over the entire deployment duration.

For statistically steady, weakly nonlinear waves, the velocity u_T, which represents water transport near Z_T, is related to velocity at $\langle Z_T\rangle$ by

$$u_T \approx \langle u|_{z=\langle Z_T\rangle}\rangle + u_{\mathrm{ID}}|_{z=\langle Z_T\rangle}, \tag{10}$$

where the velocity calculated from isotherm displacement is

$$u_{\mathrm{ID}} = \frac{\partial\langle u'Z_T'\rangle}{\partial z} \tag{11}$$

[from (4b) of McDougall and McIntosh (2001), simplified as noted between our (A1) and (A2)]. To interpret (11), first write $u_{\mathrm{ID}} = u_{nb} + u_b$, where the non-bolus velocity

$$u_{nb} = \langle(\partial u'/\partial z)Z_T'\rangle, \tag{12}$$

and the bolus velocity

$$u_b = \langle u'(\partial Z_T'/\partial z)\rangle. \tag{13}$$

The origins of u_{nb} and u_b are illustrated in Figs. 4a and 4b for the mode-1 wave $u = u_0\cos[2\pi(x - ct)/L]\cos(\pi z/h)$ with $u_0 \ll c$. Averaging at the moving elevation of an isotherm (Pinkel and Anderson 1997; Alford 2001; Pinkel 2008) yields a mean velocity approximately $\langle u\rangle + u_{nb}$, so u_{nb} accounts for the difference between the Eulerian mean and the mean on the isotherm (Fig. 4a; isothermal-coordinate models, which begin by averaging on isotherms, do not require u_{nb}). The transport velocity $u_T = \langle u\rangle + u_{nb} + u_b$ = (mean velocity on moving isotherm) + (bolus velocity). The bolus velocity accounts for fluctuations in layer thickness (Fig. 4b), so u_T is a "thickness-weighted mean" in the terminology of Young (2012) [the term "bolus velocity," as used here and by other researchers (e.g., Dukowicz and Greatbatch 1999), does not imply the existence of "turbulent surges" (Helfrich 1992) or "trapped cores" with $u > c$ (Flierl 1981)]. For the wave of Fig. 4, nonbolus velocity is opposite wave propagation and maximum at intermediate depths $[u_{nb} = -(u_0^2/2c)\sin^2(\pi z/h)]$, whereas bolus velocity is in the wave propagation direction and maximum near the bed and near the surface $[u_b = (u_0^2/2c)\cos^2(\pi z/h)$; Fig. 4c].

To illustrate (6)–(9), consider the flux of water with temperatures between 10° and 10.5°C, that is, $q(10.25°\mathrm{C})$

with $\Delta T = 0.5$°C. Let the lower and upper solid gray lines in Fig. 4b respectively be the 10° and 10.5°C isotherms. Now $\delta[T(t, z) - T_j]$ equals ΔT^{-1} between these isotherms, and equals zero everywhere else. From (6) and (7), q(10.25°C) is the depth-integrated, wave-averaged transport of the water between the two isotherms normalized by ΔT^{-1}, and from (9) u_T is the mean velocity of particles in this layer.

Expression (2) for the Stokes drift resembles (11) and has a similar interpretation. The distinction is the possible difference between the particle displacement Z' and the isotherm displacement Z'_T. The Stokes drift can be broken into nonbolus and bolus components by replacing Z'_T with Z' in (12) and (13). If mixing is negligible, given weakly nonlinear waves and near-vertical temperature gradients, $Z'_T = Z'$, so from (2) and (11),

$$u_T = \langle u \rangle + u_{\mathrm{ST}}; \tag{14}$$

that is, the thickness-weighted isothermal-mean velocity u_T equals the mean particle velocity [the approximations stated above may be important to (14), as is discussed further in section 6].

Both bolus and nonbolus terms contribute to the Stokes drift throughout the BBL. However, their values are modified by BBL friction [see discussion following (5)] and may differ from the frictionless case illustrated in Fig. 4. For a steadily propagating wave, the bolus velocity [second term on right of (5)] remains in the direction of wave propagation throughout the BBL. The nonbolus velocity [first term on right of (5)] is also in the direction of wave propagation within some neighborhood of the bed. Therefore, the near-bed nonbolus velocity is opposite the above-BBL nonbolus velocity (this reversal occurs because the no-slip condition ensures that $\partial u'/\partial z$ and Z' have the same sign near the bed, in contrast to the opposite signs for the above-BBL motion of Fig. 4).

Given substantial mixing, $Z'_T \neq Z'$ and u_T differs from the mean particle velocity. However, if mixing within a single wave period is substantial but limited to the BBL (as may be a good approximation given sufficiently large gradient Richardson number above the BBL), then equality between thickness-weighted isothermal-mean velocity and particle velocity still holds in a boundary layer-integrated sense. To see this, let z_+ be a fixed elevation above the boundary layer, note that $\int_0^{z_+} u_{\mathrm{ID}}\, dz = \langle u' Z'_T \rangle|_{z=z_+}$ [from (11)], $\int_0^{z_+} u_{\mathrm{ST}}\, dz = \langle u' Z' \rangle|_{z=z_+}$ [from (2)], and $Z'_T|_{z=z_+} = Z'|_{z=z_+}$ (given negligible mixing above the BBL, and other assumptions previously noted above). In this case, isothermal-mean analysis yields an estimate of the boundary layer-averaged Stokes drift:

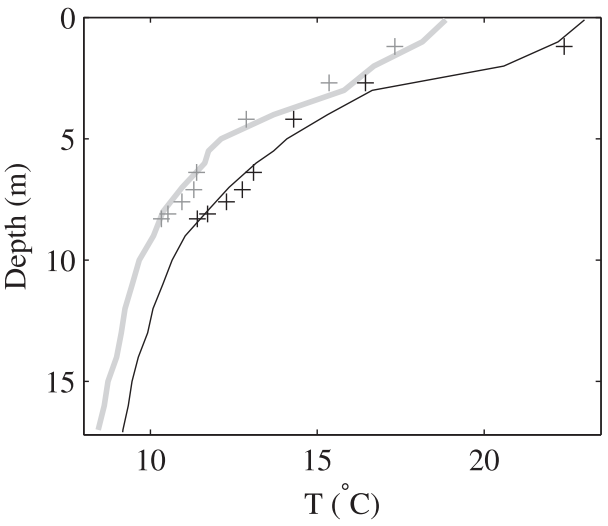

FIG. 5. Temperature profiles measured on 18 May (gray) and 11 July (black) near the lake's deepest point (solid lines) and at tripod location (pluses).

$$\overline{u}_{\mathrm{ST}} = \frac{1}{z_+} \int_{\tilde{z}=0}^{z_+} (u_T - \langle u \rangle)\, d\tilde{z}, \tag{15}$$

where z_+ was set to 1.1 m.

5. Results

a. Description of internal waves

Stratification in Lacamas Lake strengthened as the lake warmed during summer (Fig. 5). At the tripod location, between 18 May and 11 July, water temperature measured near the bed (elevation $z = 0.2$ m) and near the surface ($z = 7.3$ m) respectively increased by 1.1° and 5.0°C. At the deep water location, for depths exceeding about 3 m, the temperature gradient decreased with increasing depth. Similarly, at the tripod location, the strongest temperature gradients were measured in the upper water column (between $z = 4.3$ and 7.3 m, 24-h-averaged temperature gradients measured on 18 May and 11 July were $d\langle T \rangle/dz = 1.5$°C m^{-1} and 2.7°C m^{-1}), with weaker gradients at greater depths (between $z = 1.3$ and 4.3 m, average temperature gradients measured on 18 May and 11 July were 0.54°C m^{-1} and 0.53°C m^{-1}). However, at the tripod, this trend reversed in the BBL, where elevated mean temperature gradients were observed (between $z = 0.2$ m and 1.3 m, average temperature gradients measured on 18 May and 11 July were 0.81°C m^{-1} and 1.1°C m^{-1}). In contrast to the expectation that mixing causes weak near-bed mean stratification, the increase in BBL stratification was most marked nearest the bed (between $z = 0.2$ m and 0.4 m, average

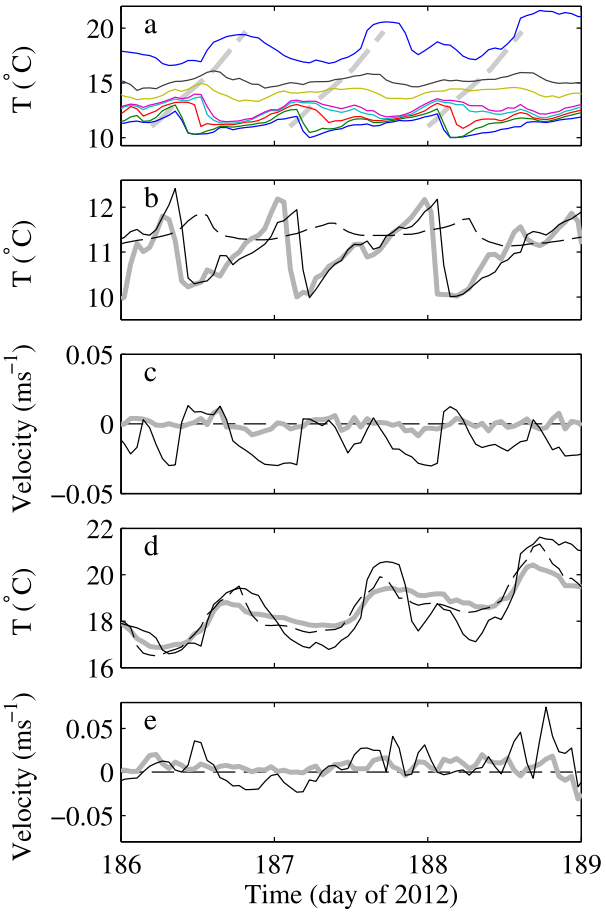

FIG. 6. Time series of hourly mean temperature and velocity. (a) Temperature from vertical instrument stack (elevations z = 0.2, 0.4, 0.9, 1.4, 2.1, 4.3, 5.8, 7.3 m) at tripod location, each curve a single instrument, with successively higher instruments recording higher temperatures. Gray dashed lines indicate theoretical upward propagation of lakewide internal wave. (b) Near-bed temperatures measured by RBR temperature loggers mounted on tripod (solid black), and by nearby deep (thick gray), and shallow (dashed black) Hobo loggers. (c) Along- (black) and across-lake (gray) velocity measured 0.15 m above bed at tripod. (d) As in (b), but for near-surface temperatures. (e) As in (c), but for near-surface velocity.

temperature gradients measured on 18 May and 11 July were 0.97°C m^{-1} and 1.5°C m^{-1}).

Internal waves caused the hourly mean temperature to fluctuate a few degrees (Fig. 6a). Wave-induced temperature fluctuations were dominated by frequencies between 0.75 and 2.5 cycles per day (after removing seasonal warming by subtracting a best-fit quadratic from the 48-day time series measured at z = 1.3 m, this frequency band was responsible for 78% of remaining temperature variance). Observations from the deepest part of the lake have shown upward-propagating internal waves (Henderson and Deemer 2012). At the tripod location, upward propagation is less clear. Nevertheless, a weak trend can be discerned by comparing temperature fluctuations with the theoretical propagation for the lakewide wave calculated from (1) using the energy-weighted mean frequency σ = 1.5 cycles per day [dashed gray lines, Fig. 6a; propagation toward increasing elevation mapped onto propagation toward warmer temperatures using the measured temperature profile $\langle T(z)\rangle$]. As expected given horizontal-mode-1 structure of the lakewide internal wave (Henderson and Deemer 2012), temperature fluctuations observed at the tripod (z = 1.3 m) were coherent with, but opposite to, fluctuations measured near the lake's northwest end (triangle, Fig. 1; for the band 0.75–2.5 cycles per day, bulk coherence^2 = 0.69 and phase = 160°, not shown; the 20° departure from 180° phase was consistent with estimated upward propagation speed, and the 1-m elevation difference between the two instruments).

Comparing near-bed temperature fluctuations measured at the tripod with fluctuations measured upslope and downslope of the tripod (i.e., at locations of star and diamond in Fig. 1) reveals upslope wave propagation (Fig. 6b). In the dominant 0.75–2.5 cycles per day frequency band, near-bed temperature fluctuations measured at the tripod lagged those measured 114 m downslope by 1.4 h, yielding an upslope propagation speed of 0.023 m s^{-1} [for these frequencies, cross spectra evaluated with 5 degrees of freedom (not shown) yielded phase = (360° × 1.4 h) × frequency, with r^2 of 0.87]. Outside the 0.75–2.5 cycles per day band, coherence between the two temperature time series dropped markedly (coherence^2 exceeded 0.79 for all 14 frequencies in the 0.75–2.5 cycle per day band, but for only four of 85 frequency bins outside this band; not shown).

Owing to internal bores (section 2), near-bed temperature fluctuations exhibited long intervals of slow warming, punctuated by shorter intervals of rapid cooling (Fig. 6b). This asymmetry between warming and cooling phases was greatly weakened above the BBL (Fig. 6a) because bores were confined to the near-bed region.

Hourly mean velocities fluctuated with the passage of each internal wave, with along-lake velocity dominating over across-lake velocity [Fig. 6c; here the along-lake direction, 126° clockwise from north (arrows, Fig. 1), was chosen to maximize along-lake velocity variance]. Dominance of along-lake velocity was consistent with along-lake, upslope wave propagation. At z = 0.135 and 1.0 m, respectively, frequencies between 0.75 and 2.5 cycles per day contributed fluctuations with standard deviations 0.011 and 0.020 m s^{-1} (only slightly less than the upslope phase speed of 0.023 m s^{-1}), accounting for

70% of detrended velocity variance. Weak upslope flow was associated with cold water, whereas warming occurred during downslope flow [compare Figs. 6b and 6c; for an explanation of this trend, see Deemer et al. (2015)]. Arrival of internal bores was associated with sudden transitions from downslope to upslope velocity.

Stratification often inhibited mixing (Deemer et al. 2015), as indicated by the Richardson number (Phillips 1977)

$$\mathrm{Ri} = \frac{g(\rho_l - \rho_u)(z_u - z_l)}{\rho_l[(u_l - u_u)^2 + (v_l - v_u)^2]}, \tag{16}$$

where ρ_α, u_α, and v_α are density, across-lake velocity, and along-lake velocity at elevations z_α. Above the BBL (z_l, z_u = 2.1, 4.3 m, respectively, with velocities estimated by linear interpolation of ADP data), Ri exceeded 0.25, 1, and 2 respectively in 99.9%, 94%, and 85% of cases, indicating consistent suppression of mixing by stratification (not shown). Nearer the bed, (z_l, z_u = 0.2 m, 0.4 m), Ri exceeded 0.25, 1, and 2 respectively in 91%, 48%, and 24% of cases, indicating less consistent inhibition of BBL mixing.

In contrast to the upslope propagation evident near the bed (Fig. 6b), no clear propagation is discernible from near-surface temperatures (Fig. 6d; cross-spectral analysis between laterally displaced temperature gauges revealed no clear trend, with an r^2 between frequency and cross-spectral phase of 0.04). Relationships between near-surface velocity and temperature were also unclear (Figs. 6d,e), for reasons that are unknown (forcing by fluctuating winds provides one possible explanation).

Theoretically, the observed upslope propagation of near-bed internal waves implies onshore near-bed Stokes drift, with a reversal to offshore drift higher in the water column (section 3b). The near-surface Stokes drift is difficult to predict, partly owing to the lack of clear wave propagation near the surface.

b. *Eulerian mean velocity and Stokes drift*

Steady wave propagation was assumed to derive expressions for the Stokes drift (section 3). Since clear propagation was observed only near the bed, this section presents results only for transport within 1.1 m of the bed, measured by the downward-looking ADPs. Discussion of transport through the remainder of the water column is deferred to section 5c.

Averaged over the 48-day deployment, the near-bed Eulerian velocity flowed downslope at about 0.01 m s^{-1} (thin black line, Fig. 7). If water particles were on average transported downslope at this speed, then advection of warmer water from upslope locations would cause rapid warming. BBL models neglecting Stokes drift (Garrett et al. 1993) predict mean warming at rate $\partial T/\partial t \sim \langle u\rangle(\partial T/\partial z)\sin\theta$, where θ = bed slope. Setting $\langle u\rangle$ = 0.01 m s^{-1}, $\partial T/\partial z$ = 1°C m^{-1}, and bed slope θ = 0.87° yields mean warming rate of 1.3°C day^{-1}, or 62°C over the course of the 48-day deployment. Such rapid warming was not observed (observed near-bed warming was 0.02°C day^{-1}; Fig. 5). A possible explanation is that an upslope near-bed Stokes drift, predicted in section 5a, opposed downslope particle advection.

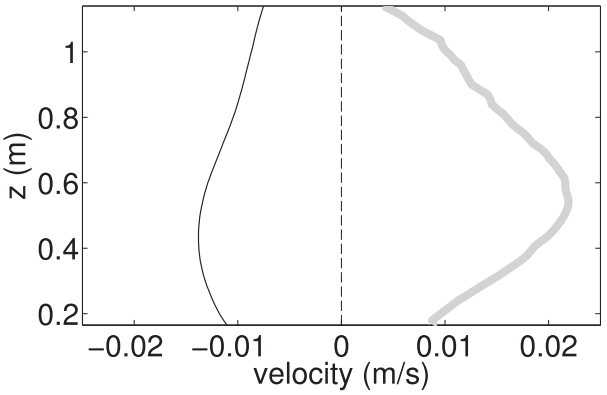

FIG. 7. Near-bed profile of along-lake Eulerian velocity (thin black line) and internal-wave Stokes drift (thick gray line) averaged over the 48-day deployment (positive velocities indicate upslope flow).

Stokes drift estimation from (2) and (3) requires an assumption of steady upslope wave propagation, but coherent propagation was observed only in the dominant frequency band 0.75–2.5 cycles per day (section 5a). When u' was calculated as the velocity contributed by this frequency band, the Stokes drift averaged over the 48-day deployment was consistent with partial cancellation of the near-bed Eulerian mean flow by the Stokes drift (thick gray line opposite thin black line, Fig. 7). Boundary layer-averaged estimated Stokes drift exceeded the Eulerian mean flow by 30%, a difference that increases if u' is not limited to the 0.75–2.5 cycles per day band (including all frequencies gives an estimated mean boundary layer–averaged Stokes drift double the mean Eulerian velocity, although this calculation is unjustified because coherence was limited at higher frequencies).

Fluctuations in Stokes drift observed during the 48-day deployment tended to oppose fluctuations in the Eulerian-mean velocity. Averaged over a 2-day running mean and from the bed to z = 1.1 m, fluctuations in Eulerian-mean velocity resembled fluctuations in Stokes drift, although scatter was considerable (compare thin black and thick gray lines in Fig. 8; by regression, boundary layer-averaged $u_{ST} = -1.4\langle u\rangle - 9 \times 10^{-4}$ m s^{-1} with r^2 = 0.46).

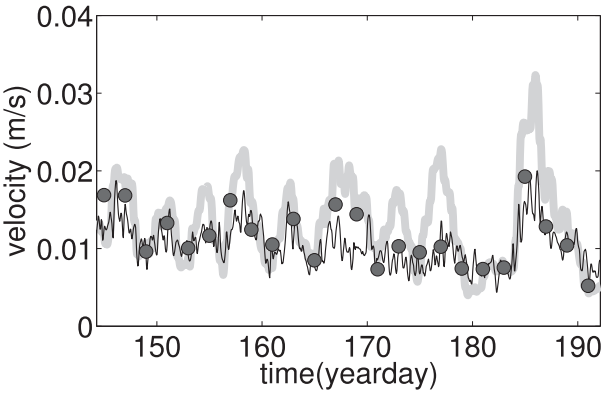

FIG. 8. Time series of wave-averaged (2-day running mean), vertically averaged (from bed to $z = 1.1$ m) downslope Eulerian velocity (thin black line) and upslope internal-wave Stokes drift. Stokes drift estimates based on weak nonlinearity and steady wave propagation [(2) and (3), thick gray line] and based on isothermal-mean analysis [(15), circles].

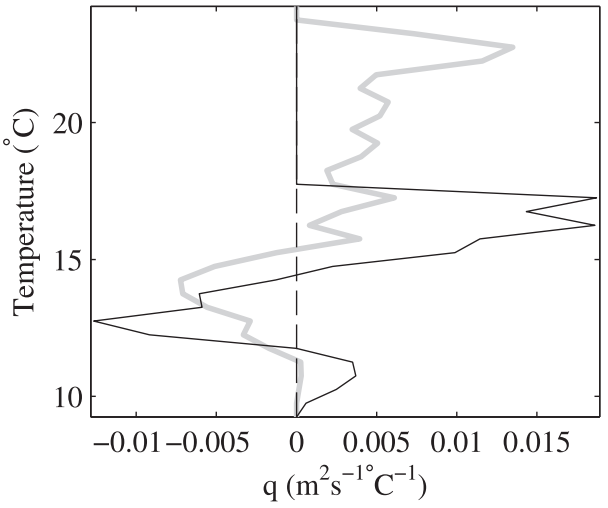

FIG. 9. Upslope isothermal transport averaged over 48 h on 4–5 June (thin black line) and 8–9 July (thick gray line).

c. *Isothermal-mean transport*

During selected 2-day intervals early and late in the deployment, the isothermal-mean flux $q(T)$ [(6)] indicates onshore transport of the warmest (near surface) water and offshore transport of intermediate-temperature water (Fig. 9). Early in the deployment, mean onshore transport of the coolest (near bed) water was also observed [$q(T) > 0$ for $T < 12$°C; thin black line, Fig. 9]. Early in the deployment, water temperatures were relatively cool, so no transport of the warmest water classes was measured [$q(T) = 0$ for $T > 18$°C; thin black line, Fig. 9]. As the lake warmed, warmer temperature classes were transported onshore, and the transport of the coolest temperature classes reduced to zero [$q(T) = 0$ for $T < 11$°C; thick gray line, Fig. 9].

To facilitate comparison with section 5b, the thickness-weighted isothermal-mean velocity u_T [(9)] was compared with the Eulerian-mean velocity (Fig. 10; the near-bed part of Eulerian velocity profile was previously shown in Fig. 7). Recall that, under simplifying assumptions and neglecting mixing, the thickness-weighted isothermal mean velocity equals the mean particle velocity [i.e., equals Eulerian-mean velocity plus Stokes drift; (14)]. Near the bed, the thickness-weighted isothermal-mean velocity was much less than the Eulerian mean, as expected given the tendency for cancellation of downslope Eulerian and upslope Stokes transports found in section 5b. This result, obtained by averaging over the entire experiment, was supported by approximate cancelation of BBL-averaged, 2-day-running-mean $\langle u \rangle$ and $\overline{u}_{\mathrm{ST}}$ [compare thin black line with circles, Fig. 8; $\overline{u}_{\mathrm{ST}}$ defined by (15)]. This finding can be restated as follows: the wave-averaged transport, integrated over the coolest water classes, was much smaller than expected given the wave-averaged downslope Eulerian velocity, and transport remained consistently small despite substantial fluctuations in Eulerian velocity. The Stokes drift estimated from isothermal-mean analysis, $\overline{u}_{\mathrm{ST}}$, cancels the Eulerian mean flow more exactly than the Stokes drift estimated in section 5b, possibly owing to errors in steady-propagation and weak-nonlinearity assumptions. At middepths, the thickness-weighted isothermal-mean velocity was offshore of Eulerian mean, indicating reversal of the Stokes drift (Fig. 10; such a reversal is expected from theory; section 3). Near the surface, where along-lake wave propagation was unclear (section 5a), isothermal- and Eulerian-mean velocities did not differ greatly (indicating minimal Stokes drift), and a shoreward Eulerian mean flow transported warm water onshore.

6. Discussion

The near-bed Stokes drift of internal waves propagating up a sloping lakebed has been found to oppose a downslope Eulerian-mean velocity, as has been predicted on theoretical grounds (Wunsch 1971; Ou and Maas 1986; Garrett et al. 1993). Opposition of BBL-integrated Stokes and Eulerian transports results from the kinematics of density conservation, and is independent of the forces responsible for generating the Eulerian-mean flow. Indeed, the observations presented here do not resolve mean forcing terms, which might include isopycnal setup (Umeyama and Shintani 2014), wave-induced momentum fluxes (Longuet-Higgins 1953; Bordes et al. 2012; Grisouard and Bühler 2012; Pinkel

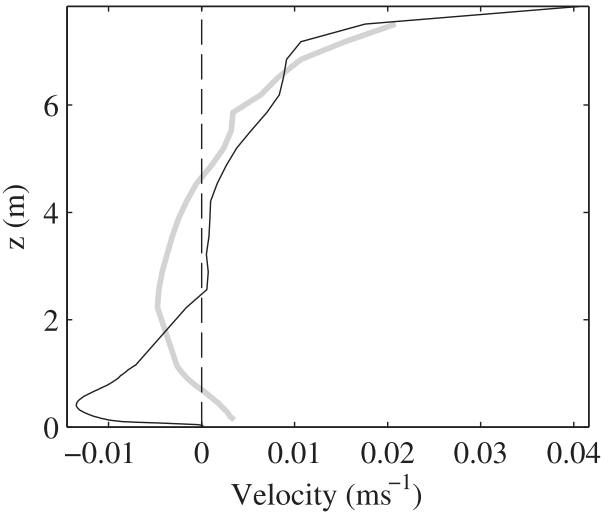

FIG. 10. Eulerian-mean (thin black line) and thickness-weighted isothermal-mean (thick gray line) velocity profiles, averaged over the 48-day deployment. Eulerian velocity interpolated between $z = 1.14$ and 2.23 m. To calculate the plotted thickness-weighted isothermal-mean velocity, time series of 2-day running mean of u_T were calculated using (9), and then averaged over the entire deployment.

et al. 2012), and turbulent Reynolds stresses. Understanding of this environment may be improved by further research into forcing of mean currents. However, even in other environments subjected to different forcing, the kinematic results emphasized here may apply. Upslope near-bed Stokes drift is a general property of steady upslope propagation, and upslope-propagating internal waves are often observed over sloping beds in lakes (Imberger 1998; Thorpe and Lemmin 1999) and oceans (Hosegood and van Haren 2004; Bluteau et al. 2011; Walter et al. 2014).

Isothermal-mean analysis revealed a residual onshore flux of warm near-surface water, an offshore flux of underlying intermediate water, and a weak onshore flux of the coldest water. The implied Stokes drift reversed, from onshore near the bed to offshore in the midwater column, consistent with theoretical expectations (section 3b). Near the surface, wave propagation was unclear and the Stokes drift was small.

Owing to the downslope Eulerian mean flow, near-bed downslope flows tended to have higher speeds than upslope flows (e.g., thin black line, Fig. 6c). One expected consequence is a downslope mean bed stress, which may influence sediment transport (cf. Butman 1988). An additional expected consequence is enhancement of turbulence during downslope flow. Averaged over the entire deployment, the cube of near-bed water speed (i.e., $|u|^3$ at $z = 0.135$ m), to which turbulent dissipation may be proportional (Henderson 2016), was 2.7 times greater during downslope flow than during upslope flow. Since BBL shear intensifies stratification and chemical gradients during downslope flows (Lorke et al. 2005; Deemer et al. 2015), high speeds coincide with strong gradients, possibly increasing the effectiveness of BBL mixing.

As noted in section 1, BBL models that neglect wave-induced fluxes predict upslope transport of the coldest water in the inner boundary layer, and downslope transport of warmer water in the outer boundary layer (Phillips et al. 1986; Garrett et al. 1993; Umlauf and Burchard 2011). Here, in the presence of substantial Stokes drift, the thickness-weighted isothermal-mean velocity profile resembled these predictions in the sense that the coldest water was advected upslope and slightly warmer water was advected downslope (e.g., consider the bottom meter of the u_T profile in Fig. 10). However, in contrast to the mixing-induced reduction in mean near-bed stratification predicted by previous models, the observed mean stratification intensified within 0.4 m of the bed. To clarify the potential significance of this result, consider two processes that might reduce the importance of BBL mixing to basinwide stratification (Garrett et al. 1993). First, the efficiency of BBL mixing would be low if BBL stratification were weak. Second, the partial cancelation of mixing by advective buoyancy fluxes predicted by modeling studies (section 1) would be absent if stratification were not reduced in the BBL. To address the interaction between BBL mixing and mean advection, further work to examine mean stratification very near the bed, and the role of wave nonlinearity and time-dependent mixing, may prove valuable.

Several assumptions were necessary to derive the simple results of sections 3 and 4. Readers seeking generalizations are referred to Middleton and Loder (1989) and Plumb (1979) for three-dimensional flows and relaxation of the steady-propagation assumption; to Andrews and McIntyre (1978) and Flierl (1981) for mean particle motions in strongly nonlinear waves; to Walin (1977, 1982), McDougall and McIntosh (2001), Young (2012), and Groeskamp et al. (2014) for isopycnal-mean analysis; and to Giddings et al. (2014) for related sigma-coordinate analysis. For isothermal-mean analysis (sections 4 and 5c), the neglect of across-lake motions may be particularly significant. Such motions introduce a neglected Stokes drift contribution $\partial\langle u'Y'\rangle/\partial y$ (where y and Y' are across-lake position and displacement), which can be interpreted in a manner similar to the resolved $\partial\langle u'Z'\rangle/\partial z$ term (Middleton and Loder 1989). The Eulerian mean velocity may also vary in the across-lake direction (horizontal circulation is possible). Such neglected across-lake variability is likely

smaller than Eulerian and Stokes velocities, as evidenced by their near-cancelation (compare black line and circles, Fig. 8). However, since BBL-integrated Eulerian and Stokes velocities almost cancel, across-lake variability might be substantial compared with the small net transport. The Stokes drift estimates of sections 3 and 5b required assumptions of steady propagation and weak nonlinearity that were not required for isothermal analysis. Comparison with isothermal analysis suggests that these assumptions introduced errors of 30%–40%.

The analysis applied here required only conventional measurements: velocity profiles for the evaluation of Stokes drift under steadily propagating waves, and combined velocity and temperature profiles for evaluation of isothermal-mean transport. Similar analysis can be envisaged in other limnologic or oceanographic cases, although potential difficulties include strong nonlinearity and departures from steady propagation (for Stokes drift estimation), three-dimensionality (which complicates both Stokes drift and isothermal-mean analysis), and the possibility that residual means may be unmeasurably small.

Acknowledgments. John Harrison and Bridget Deemer contributed to planning and execution of fieldwork, and provided valuable comments on this manuscript. Further fieldwork assistance was provided by Abby Lunstrum, Homer Adams, Andrew Harwood, Alyson Day, Joshua Arnold, and Matthew Schultt. Funding was provided by the National Science Foundation Awards 1045286 and 1355211, and by U.S. Geological Survey Award 06HQGR0126.

APPENDIX

Expression for Stokes Drift

Approximating the velocity near (x_0, z_0) as a linear function of x and z yields

$$\Delta u \approx X' \frac{\partial u}{\partial x}\bigg|_{x=x_0,z=z_0} + Z' \frac{\partial u}{\partial z}\bigg|_{x=x_0,z=z_0}, \qquad \text{(A1)}$$

where (X', Z') are the wave-induced particle displacements from (x_0, z_0) and, for any variable ξ, the notation $\xi|_{x=x_0,z=z_0}$ indicates ξ evaluated at (x_0, z_0) [for the perturbation expansion justifying (A1), see section 3.3 of Phillips (1977)]. Let (u', w') be wave-induced velocity fluctuations at fixed location (x_0, z_0), so $(u, w) = (\langle u\rangle, \langle w\rangle) + (u', w')$. Next, u in (A1) is approximated by u', which is usually justified unless waves are much weaker than mean currents [because the term $(\partial\langle u\rangle/\partial z)\langle Z'^2\rangle/2$ in (3) of McDougall and McIntosh (2001) is third order if $(\partial\langle u\rangle/\partial x, \partial\langle u\rangle/\partial z)$ is of order $(\partial u'/\partial x, \partial u'/\partial z)$]. Now averaging (A1) gives

$$u_{\mathrm{ST}} \approx \left\langle X' \frac{\partial u'}{\partial x} \right\rangle + \left\langle Z' \frac{\partial u'}{\partial z} \right\rangle. \qquad \text{(A2)}$$

The derivation of (2) from (A2) follows previous more general analysis (e.g., Middleton and Loder 1989). Specifically,

$$\begin{aligned}\langle X'(\partial u'/\partial x)\rangle &= \partial\langle X'u'\rangle/\partial x - \langle u'(\partial X'/\partial x)\rangle \\ &= (1/2)\partial^2\langle X'^2\rangle/\partial t\partial x - \langle u'(\partial X'/\partial x)\rangle \\ &= -\langle u'(\partial X'/\partial x)\rangle = \langle u'(\partial Z'/\partial z)\rangle,\end{aligned}$$

where the second equality follows from $u' \approx \partial X'/\partial t$, the third from statistically steady flow, and the fourth from mass conservation. Physically, given statistically steady wave field, the correspondence between the lateral displacement component of the Stokes drift (left of equations) and the bolus velocity (right of final equation) occurs because particles must converge laterally ($\partial X/\partial x < 0$) for a layer to thicken ($\partial Z/\partial z < 0$). Substituting the final form into (A2) yields (2).

REFERENCES

Alford, M., 2001: Fine-structure contamination: Observations and a model of a simple two-wave case. *J. Phys. Oceanogr.*, **31**, 2645–2649, doi:10.1175/1520-0485(2001)031<2645:FSCOAA>2.0.CO;2.

Andrews, D., and M. McIntyre, 1978: An exact theory of nonlinear waves on a Lagrangian-mean flow. *J. Fluid Mech.*, **89**, 609–646, doi:10.1017/S0022112078002773.

Bluteau, C., N. Jones, and G. Ivey, 2011: Dynamics of a tidally-forced stratified shear flow on the continental slope. *J. Geophys. Res.*, **116**, C11017, doi:10.1029/2011JC007214.

Boegman, L., 2009: Currents in stratified water bodies. 2: Internal waves. *Encyclopedia of Inland Waters*, L. Boegman, Ed., Academic Press, 539–558.

——, G. Ivey, and J. Imberger, 2005a: The degeneration of internal waves in lakes with sloping topography. *Limnol. Oceanogr.*, **50**, 1620–1637, doi:10.4319/lo.2005.50.5.1620.

——, ——, and ——, 2005b: The energetics of large-scale internal wave degeneration in lakes. *J. Fluid Mech.*, **531**, 159–180, doi:10.1017/S0022112005003915.

Bordes, G., A. Venaille, S. Joubaud, P. Odier, and D. Thierry, 2012: Experimental observation of a strong mean flow induced by internal gravity waves. *Phys. Fluids*, **24**, 086602, doi:10.1063/1.4745880.

Bryden, H. L., J. Candela, and T. H. Kinder, 1994: Exchange through the Strait of Gibraltar. *Prog. Oceanogr.*, **33**, 201–248, doi:10.1016/0079-6611(94)90028-0.

Butman, B., 1988: Downslope Eulerian mean flow associated with high-frequency current fluctuations observed on the outer continental shelf and upper slope along the northeastern United States continental margin: Implications for sediment transport. *Cont. Shelf Res.*, **8**, 811–840, doi:10.1016/0278-4343(88)90078-7.

Cossu, R., and M. G. Wells, 2013: The interaction of large amplitude internal seiches with a shallow sloping lakebed: Observations of benthic turbulence in Lake Simcoe, Ontario, Canada. *PLoS One*, **8**, e57444, doi:10.1371/journal.pone.0057444.

Deemer, B. R., S. M. Henderson, and J. A. Harrison, 2015: Chemical mixing in the bottom boundary layer of a eutrophic reservoir: The effects of internal seiching on nitrogen dynamics. *Limnol. Oceanogr.*, **60**, 1642–1655, doi:10.1002/lno.10125.

Dukowicz, J. K., and R. J. Greatbatch, 1999: The bolus velocity in the stochastic theory of ocean turbulent tracer transport. *J. Phys. Oceanogr.*, **29**, 2232–2239, doi:10.1175/1520-0485(1999)029<2232:TBVITS>2.0.CO;2.

Flierl, G. R., 1981: Particle motions in large-amplitude wave fields. *Geophys. Astrophys. Fluid Dyn.*, **18**, 39–74, doi:10.1080/03091928108208773.

Garrett, C., P. MacCready, and P. Rhines, 1993: Boundary mixing and arrested Ekman layers: Rotating stratified flow near a sloping boundary. *Annu. Rev. Fluid Mech.*, **25**, 291–323, doi:10.1146/annurev.fl.25.010193.001451.

Giddings, S. N., S. G. Monismith, D. A. Fong, and M. T. Stacey, 2014: Using depth-normalized coordinates to examine mass transport residual circulation in estuaries with large tidal amplitude relative to the mean depth. *J. Phys. Oceanogr.*, **44**, 128–148, doi:10.1175/JPO-D-12-0201.1.

Goudsmit, G.-H., F. Peeters, M. Gloor, and A. Wuest, 1997: Boundary mixing versus internal diapycnal mixing in stratified natural waters. *J. Geophys. Res.*, **102**, 27 903–27 914, doi:10.1029/97JC01861.

Grisouard, N., and O. Bühler, 2012: Forcing of oceanic mean flows by dissipating internal tides. *J. Fluid Mech.*, **708**, 250–278, doi:10.1017/jfm.2012.303.

Groeskamp, S., J. D. Zika, T. McDougal, B. M. Sloyan, and F. Laliberté, 2014: The representation of oceanic circulation and variability in thermodynamic coordinates. *J. Phys. Oceanogr.*, **44**, 1735–1750, doi:10.1175/JPO-D-13-0213.1.

Helfrich, K. R., 1992: Internal solitary wave breaking and run-up on a uniform slope. *J. Fluid Mech.*, **243**, 133–154, doi:10.1017/S0022112092002660.

Henderson, S. M., 2016: Turbulent production in an internal wave bottom boundary layer maintained by a vertically propagating seiche. *J. Geophys. Res.*, **121**, doi:10.1002/2015JC011071, in press.

——, and B. R. Deemer, 2012: Vertical propagation of lakewide internal waves. *Geophys. Res. Lett.*, **39**, L06405, doi:10.1029/2011GL050534.

Horn, D., J. Imberger, and G. Ivey, 2001: The degeneration of large-scale interfacial gravity waves in lakes. *J. Fluid Mech.*, **434**, 181–207, doi:10.1017/S0022112001003536.

Hosegood, P., and H. van Haren, 2004: Near-bed solibores over the continental slope in the Faeroe-Shetland Channel. *Deep Sea Res. II*, **51**, 2943–2971, doi:10.1016/j.dsr2.2004.09.016.

Huthnance, J. M., 1995: Circulation, exchange and water masses at the ocean margin: The role of physical processes at the shelf edge. *Prog. Oceanogr.*, **35**, 353–431, doi:10.1016/0079-6611(95)80003-C.

Imberger, J., 1998: Flux paths in a stratified lake: A review. *Physical Processes in Lakes and Oceans*, J. Imberger, Ed., Amer. Geophys. Union, 1–17.

Inall, M. E., 2009: Internal wave induced dispersion and mixing on a sloping boundary. *Geophys. Res. Lett.*, **36**, L05604, doi:10.1029/2008GL036849.

——, G. Shapiro, and T. Sherwin, 2001: Mass transport by nonlinear internal waves on the Malin Shelf. *Cont. Shelf Res.*, **21**, 1449–1472, doi:10.1016/S0278-4343(01)00020-6.

Klymak, J. M., and J. N. Moum, 2003: Internal solitary waves of elevation advancing on a shoaling shelf. *J. Geophys. Res.*, **30**, 2045, doi:10.1029/2003GL017706.

Lamb, K. G., 1997: Particle transport by nonbreaking, solitary internal waves. *J. Geophys. Res.*, **102**, 18 641–18 660, doi:10.1029/97JC00441.

Ledwell, J. R., A. J. Watson, and C. S. Law, 1993: Evidence for slow mixing across the pycnocline from an open-ocean tracer-release experiment. *Nature*, **364**, 701–703, doi:10.1038/364701a0.

Lohrmann, A., B. Hackett, and L. P. Roed, 1990: High resolution measurements of turbulence, velocity, and stress using pulse-to-pulse coherent sonar. *J. Atmos. Oceanic Technol.*, **7**, 19–37, doi:10.1175/1520-0426(1990)007<0019:HRMOTV>2.0.CO;2.

Longuet-Higgins, M., 1953: Mass transport in water waves. *Philos. Trans. Roy. Soc. London*, **245A**, 535–581, doi:10.1098/rsta.1953.0006.

Lorke, A., F. Peeters, and A. Wüest, 2005: Shear-induced convective mixing in bottom boundary layers on slopes. *Limnol. Oceanogr.*, **50**, 1612–1619, doi:10.4319/lo.2005.50.5.1612.

MacCready, P., 2011: Calculating estuarine exchange flow using isohaline coordinates. *J. Phys. Oceanogr.*, **41**, 1116–1124, doi:10.1175/2011JPO4517.1.

MacDonald, D. G., 2006: Estimating an estuarine mixing and exchange ratio from boundary data with application to Mt. Hope Bay (Massachusetts/Rhode Island). *Estuarine Coastal Shelf Sci.*, **70**, 326–332, doi:10.1016/j.ecss.2006.06.025.

McDougall, T. J., and P. C. McIntosh, 2001: The temporal-residual-mean velocity. Part II: Isopycnal interpretation and the tracer and momentum equations. *J. Phys. Oceanogr.*, **31**, 1222–1246, doi:10.1175/1520-0485(2001)031<1222:TTRMVP>2.0.CO;2.

Middleton, J. F., and J. W. Loder, 1989: Skew fluxes in polarized wave fields. *J. Phys. Oceanogr.*, **19**, 68–76, doi:10.1175/1520-0485(1989)019<0068:SFIPWF>2.0.CO;2.

Ou, H. W., and L. Maas, 1986: Tidal-induced buoyancy flux and mean transverse circulation. *Cont. Shelf Res.*, **5**, 611–628, doi:10.1016/0278-4343(86)90096-8.

Phillips, O., 1977: *The Dynamics of the Upper Ocean.* 2nd ed. Cambridge University Press, 344 pp.

——, J.-H. Shyu, and H. Salmun, 1986: An experiment on boundary mixing: Mean circulation and transport rates. *J. Fluid Mech.*, **173**, 473–499, doi:10.1017/S0022112086001234.

Pineda, J., 1999: Circulation and larval distribution in internal tidal bore warm fronts. *Limnol. Oceanogr.*, **44**, 1400–1414, doi:10.4319/lo.1999.44.6.1400.

Pingree, R., and B. Le Cann, 1989: Celtic and Amorican slope and shelf residual currents. *Prog. Oceanogr.*, **23**, 303–338, doi:10.1016/0079-6611(89)90003-7.

Pinkel, R., 2008: Advection, phase distortion, and the frequency spectrum of finescale fields in the sea. *J. Phys. Oceanogr.*, **38**, 291–313, doi:10.1175/2007JPO3559.1.

——, and S. Anderson, 1997: Shear, strain, and Richardson number variations in the thermocline. Part I: Statistical description. *J. Phys. Oceanogr.*, **27**, 264–281, doi:10.1175/1520-0485(1997)027<0264:SSARNV>2.0.CO;2.

——, L. Rainville, and J. Klymak, 2012: Semidiurnal baroclinic wave momentum fluxes at Kaena Ridge, Hawaii. *J. Phys. Oceanogr.*, **42**, 1249–1269, doi:10.1175/JPO-D-11-0124.1.

Plumb, R. A., 1979: Eddy fluxes of conserved quantities by small-amplitude waves. *J. Atmos. Sci.*, **36**, 1699–1704, doi:10.1175/1520-0469(1979)036<1699:EFOCQB>2.0.CO;2.

Tabaei, A., T. Akylas, and K. G. Lamb, 2005: Nonlinear effects in reflecting and colliding internal wave beams. *J. Fluid Mech.*, **526**, 217–243, doi:10.1017/S0022112004002769.

Thorpe, S., 1971: Asymmetry of the internal seiche in Loch Ness. *Nature*, **231**, 306–308, doi:10.1038/231306a0.

——, 1974: Near-resonant forcing in a shallow two-layer fluid: A model for the internal surge in Loch Ness? *J. Fluid Mech.*, **63**, 509–527, doi:10.1017/S0022112074001753.

——, 1992: Thermal fronts caused by internal gravity waves reflecting from a slope. *J. Phys. Oceanogr.*, **22**, 105–108, doi:10.1175/1520-0485(1992)022<0105:TFCBIG>2.0.CO;2.

——, 1997: On the interactions of internal waves reflecting from slopes. *J. Phys. Oceanogr.*, **27**, 2072–2078, doi:10.1175/1520-0485(1997)027<2072:OTIOIW>2.0.CO;2.

——, 1999: The generation of alongslope currents by breaking internal waves. *J. Phys. Oceanogr.*, **29**, 29–38, doi:10.1175/1520-0485(1999)029<0029:TGOACB>2.0.CO;2.

——, and U. Lemmin, 1999: Internal waves and temperature fronts on slopes. *Ann. Geophys.*, **17**, 1227–1234, doi:10.1007/s00585-999-1227-6.

Umeyama, M., and T. Shintani, 2014: Transformation, attenuation, setup, and undertow of internal waves on a gentle slope. *J. Waterway Port Coastal Ocean Eng.*, **132**, 477–486, doi:10.1061/(ASCE)0733-950X(2006)132:6(477).

Umlauf, L., and H. Burchard, 2011: Diapycnal transport and mixing efficiency in stratified boundary layers near sloping topography. *J. Phys. Oceanogr.*, **41**, 329–345, doi:10.1175/2010JPO4438.1.

Wain, D. J., and C. R. Rehmann, 2010: Transport by an intrusion generated by boundary mixing in a lake. *Water Resour. Res.*, **46**, W08517, doi:10.1029/2009WR008391.

Walin, G., 1977: A theoretical framework for the description of estuaries. *Tellus*, **29A**, 128–136, doi:10.1111/j.2153-3490.1977.tb00716.x.

——, 1982: On the relation between sea-surface heat flow and thermal circulation in the ocean. *Tellus*, **34A**, 187–195, doi:10.1111/j.2153-3490.1982.tb01806.x.

Walter, R. K., C. B. Woodson, P. R. Leary, and S. G. Monismith, 2014: Connecting wind-driven upwelling and offshore stratification to nearshore internal bores and oxygen variability. *J. Geophys. Res. Oceans*, **119**, 3517–3534, doi:10.1002/2014JC009998.

Weber, J. E. H., K. H. Christensen, and G. Bröstrom, 2014: Stokes drift in internal equatorial Kelvin waves: Continuous stratification versus two-layer models. *J. Phys. Oceanogr.*, **44**, 591–599, doi:10.1175/JPO-D-13-0135.1.

Wunsch, C., 1971: Note on some Reynolds stress effects of internal waves on slopes. *Deep Sea Res.*, **7**, 583–591, doi:10.1016/0011-7471(71)90124-0.

Young, W. R., 2012: An exact thickness-weighted average formulation of the Boussinesq equations. *J. Phys. Oceanogr.*, **42**, 692–707, doi:10.1175/JPO-D-11-0102.1.

Zhang, S., M. Alford, and J. B. Mickett, 2015: Characteristics, generation and mass transport of nonlinear internal waves on the Washington continental shelf. *J. Geophys. Res. Oceans*, **120**, 741–758, doi:10.1002/2014JC010393.

Zhou, Q., and P. J. Diamessis, 2015: Lagrangian flows within reflecting internal waves at a horizontal free-slip surface. *Phys. Fluids*, **27**, 126601, http://dx.doi.org/10.1063/1.4936578.